

Electron spin inversion in fluorinated graphene nanoribbons

Bartłomiej Rzeszutarski, Alina Mreńca-Kolasińska, and Bartłomiej Szafran
*AGH University of Science and Technology,
Faculty of Physics and Applied Computer Science,
al. Mickiewicza 30, 30-059 Kraków, Poland*

We consider a dilute fluorinated graphene nanoribbon as a spin-active element. The fluorine adatoms introduce a local spin-orbit Rashba interaction that induces spin-precession for electron passing by. The spin precession involving a single adatom is infinitesimal and accumulation of the spin precession events with many electron passages under adatoms is necessary to accomplish a spin flip. In order to arrange for this accumulation a circular n-p junction can be introduced to the ribbon by e.g. potential of the tip of an atomic force microscope. Alternatively a fluorinated quantum ring can be attached to the ribbon. We demonstrate that the spin-flip probability can be increased in this manner by as much as three orders of magnitude. The Zeeman interaction introduces spin-dependence of the Fermi wave vectors which changes the electron paths within the disordered system depending on the spin orientation. The effect destroys the accumulation of the spin precession events in the n-p junction. For side attached quantum rings however - for which the electron path is determined by the confinement within the channel - the accumulation of the spin precession is robust against the Zeeman spin splitting.

I. INTRODUCTION

The coherent spin transport in semiconducting materials [1] is under extensive studies since the idea for the spin transistor was introduced [2]. Graphene [3] due to the absence of hyperfine interactions and long spin coherence times [4, 5] is a good candidate for a spin conductor. However, pristine graphene is a poor material for spin-active elements due to the weakness of the spin-orbit interaction [6, 7]. Enhancement of the spin-orbit coupling was proposed by deposition of graphene on transition metal dichalcogenides (TMDC) [8, 9]. The coupling with the TMDC layer gives rise to a strong Rashba interaction [9] that accompany redistribution of the electron charge density and an appearance of the electric field component perpendicular to the graphene plane. Alternatively, the spin-orbit interaction can be introduced by adatoms [10], hydrogen [11–17] or fluorine [18–24]. The latter is ten times more efficient than the former as the source of the spin-orbit coupling [22].

In this paper we consider transport across the graphene nanoribbon [25] with a dilute fluorinated segment as a spin inverter of the Fermi level electrons that could be implemented as a spin transistor channel [2]. The procedure to detect the spin flips on the electron motion within the spin-orbit coupled medium was recently demonstrated [26]. The system [26] employs two quantum point contacts which are transparent to a single spin direction only. The rotation of the electron spin on the way from one contact to the other results in the conductance drop.

We study the effects of the spin precession induced by the Rashba interaction near the adatoms. We find that in the absence of the external magnetic field the spin-flip probability is very low, which we attribute to cancellation of the spin precession effects by multiple electron backscattering since the direction of the spin precession in the Rashba field depends on the orientation of the electron momentum [2].

In order to strengthen the spin-orbit coupling effects we introduce an n-p junction in an external magnetic field. The n-p junctions in graphene can be induced by electrostatic potential which moves the Dirac point above or below the Fermi level [3]. In the quantum Hall conditions these junctions form waveguides that confine currents [27–34]. The confinement in the classical terms can be understood as a result of the Lorentz force pushing the electrons to the n-p junction at both its sides. The opposite orientation of the Lorentz force for the carriers of the conduction and valence band in classical terms produces snake-orbits [32–40] winding along the junction. The magnetic confinement of the current along the junction is supported for a single direction of the current only. The effects of the spin-precession by the local Rashba interaction can be accumulated provided that the Fermi level electron passes many times under adatoms with weak backscattering. In order to recycle the electron passages we consider a circular n-p junction defined by e.g. an external gate of the scanning probe microscope [41–45]. In the quantum Hall conditions the current comes to the junction from the edge and the lifetime of the localized resonances with the current circulation around the ring can be controlled by the gate potential, the Fermi energy [44] and the external magnetic field [45]. We find that for the current circulating around the junction the spin-flip probability on the electron transfer can be increased by as much as three orders of magnitude.

We also consider the fluorinated ribbon in the quantum Hall conditions with the external potential removed. In strong magnetic fields the localized resonances are associated with the current circulation from one adatom to the other and no backscattering along the path of incidence is possible. In these conditions for a number of magnetic field values the spin-flip probability produces high peaks. For low magnetic field we find a dip of conductance which is a signature of the weak localization effects that in graphene are present when the inter-

valley scattering is strong [46]. In the present problem the adatoms as atomic scale perturbations to the lattice introduce strong intervalley scattering centers.

The effects of the accumulation of multiple spin flips requires that the electron trajectory remains unaffected by the spin orientation. The dependence of the trajectory within the disordered system on the spin orientation appears via the Zeeman interaction and the resulting spin dependence of the Fermi wave vector. In order to preserve large spin-flip probability the electron path across the fluorinated area needs to be weakly dependent on the wave vector. We show that this can be achieved with a fluorinated quantum ring side-attached to the ribbon. For one of the perpendicular magnetic field orientations the Fermi level wave function is injected to the ring provided that the Fermi energy is in resonance with states circulating within the ring [45]. The resulting spin precession is stable against the spin Zeeman interaction. Quantum rings are defined in graphene ribbons with a well established by etching techniques [47–51] and the role of the magnetic focusing has been discussed recently [45, 51].

II. THEORY

A. Hamiltonian

We use the atomistic π band tight-binding Hamiltonian, which in the absence of the fluorine adatoms takes the form

$$H_0 = \sum_{i,\sigma} W_i c_{i,\sigma}^\dagger c_{i,\sigma} + \sum_{\langle i,j \rangle} \sum_{\sigma} (t_{ij} c_{i,\sigma}^\dagger c_{j,\sigma} + H.c.) \quad (1)$$

where $c_{i,\sigma}^\dagger$ and $c_{i,\sigma}$ are the creation and annihilation operators for the electron on i -th ion with spin σ . The first sum introduces the external potential at the position of the i -th ion. The energy level corresponding to p_z orbital is taken as the reference energy level. In the second summation $\langle i,j \rangle$ runs over nearest neighbor carbon atoms and $t = -2.7$ eV is the hopping parameter.

We consider a nanoribbon which in the absence of the adatoms is a strip of a crystal lattice of a finite width (see Fig. 1(a)). The experiments on graphene ribbons indicate a presence of the transport gap [52–54] near the charge neutrality point within which the system does not conduct electrical current. For that reason we consider here a semiconducting armchair ribbon. For the proof of principle in section III.A we take a ribbon that contains only 3 carbon atoms on its width. The rest of the results is obtained either for a thinner ribbon with 292 atoms across the width of $\simeq 35$ nm (subsections III.B, III.C, III.D, and III.F) or for a wider ribbon (subsection III.E) with 1017 atoms across the width of $\simeq 125$ nm. For the thinner (wider) ribbon the scattering region considered in this work is a central finite region 85.2 nm (127 nm) long with fluorine 400 (2165) adatoms in a dilute concentration. We also consider spin rotation within

a fluorinated quantum ring of a circumference 283 nm [subsection III.F].

The locations of the fluorine atoms are generated at random with a uniform distribution. The results presented below are typical and quantitatively independent of the specific distribution. The position of the conductance peaks changes from one distribution to the other but the discussed physics does not. The fluorine atoms once adsorbed by graphene can only diffuse on its surface provided that the thermal excitations overcome migration barrier which for the fluorine adatoms is equal to 0.29 eV [55]. Therefore, the motion of the fluorine adatoms on the surface is frozen at low temperatures. The value changes with the carrier density level [56], but below we consider mainly conditions of the lowest subband transport, i.e. low Fermi energies near the charge neutrality point.

A fluorine adatom [see Fig. 1(b)] introduces additional terms to the Hamiltonian [22],

$$H' = H_0 + H_F + H_{SO}, \quad (2)$$

where H_F stands for the orbital, and H_{SO} the spin-orbit coupling effects. The orbital contribution H_F covers the level localized at the fluorine adatom (F) with the energy level $\varepsilon_f = -2.2$ eV and the hopping element $T = 5.5$ eV between the fluorine and the carbon atom (A) that form a vertical dimer ($F - A$, see Fig. 1(b)):

$$H_F = \varepsilon_f \sum_{\sigma} \hat{F}_{\sigma}^{\dagger} \hat{F}_{\sigma} + T \sum_{\sigma} (\hat{F}_{\sigma}^{\dagger} \hat{A}_{\sigma} + \hat{A}_{\sigma}^{\dagger} \hat{F}_{\sigma}), \quad (3)$$

where \hat{F}_{σ} is the annihilation operator for electron in the fluorine ion with spin σ , and A_{σ} is the annihilation operator for the fluorinated carbon atom.

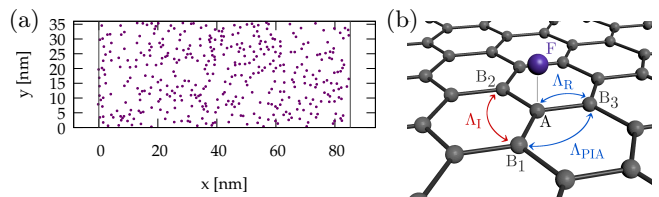


FIG. 1. (a) The considered graphene nanoribbon with 292 atoms across and the fluorinated segment. About 400 F adatoms are deposited at random (dots) within a part of nanoribbon that is 85.2 nm long. For the scattering problem the electron is incident from the left. The pristine graphene ends of the ribbon are treated as the leads feeding and draining the charge and spin current from the system. (b) The fluorine adatom and its surroundings. The symbols refer to the local spin-orbit coupling Hamiltonian introduced with the adatom H_{SO} – see Eq. (4).

The three next nearest neighbor atoms of the fluorinated carbon A are denoted by B (see Fig. 1). The annihilation operator for the electron in the B atoms is $\hat{B}_{i,\sigma}^\dagger$.

With this notation the spin-orbital part has the form [22]

$$\begin{aligned}
H_{SO} = & \frac{i\Lambda_I^B}{3\sqrt{3}} \sum_{\langle\langle i,j \rangle\rangle} \sum_{\sigma} \hat{B}_{i,\sigma}^\dagger \nu_{ij} (\hat{\mathbf{s}}_z)_{\sigma\sigma} \hat{B}_{j,\sigma} \\
& + \frac{2i\Lambda_R}{3} \sum_{B_j \in C_{nn}} \sum_{\sigma \neq \sigma'} [\hat{A}_\sigma^\dagger (\hat{\mathbf{s}} \times \mathbf{d}_{Aj})_{z,\sigma\sigma'} \hat{B}_{j,\sigma'} + \text{H.c.}] \\
& + \frac{2i\Lambda_{PIA}^B}{3} \sum_{\langle\langle i,j \rangle\rangle} \sum_{\sigma \neq \sigma'} \hat{B}_{i,\sigma}^\dagger (\hat{\mathbf{s}} \times \mathbf{d}_{ji})_{z,\sigma\sigma'} \hat{B}_{j,\sigma'}. \quad (4)
\end{aligned}$$

The first sum in the intrinsic spin-orbit coupling in the Kane-Mele form [57] which is spin-diagonal. The second term describes the Rashba interaction induced by the perpendicular electric field due to the deformation of the electron density by the adatom. The last term is the pseudospin-inversion-asymmetry next-nearest neighbor term that results from deformation of the graphene lattice by the adatom [58]. The summation $\langle\langle i,j \rangle\rangle$ runs over the nearest neighbors of the fluorinated atom $\{B_1, B_2, B_3\}$. The coefficient ν_{ij} is +1 (−1) when the path from j to i via a common nearest neighbor k , $j \rightarrow k \rightarrow i$, is counterclockwise (clockwise) and \mathbf{d}_{ij} is the unit vector in the xy plane oriented from ion j to i . The applied spin-orbit coupling parameters [22] for 0.5% concentration of the fluorine atoms are $\Lambda_I^B = 3.3$ meV, $\Lambda_R = 11.2$ meV and $\Lambda_{PIA}^B = 7.3$ meV. Both the Rashba and the PIA terms induce spin variation in the electron motion across the fluorinated area. However, for the applied parameters the effect of the PIA is by an order of magnitude lower in terms of the spin-flipping transfer probability.

The orbital effects of the external perpendicular external magnetic field is introduced to the Hamiltonian by modification of the hopping parameters. For the Hamiltonian of Eq. (2) put in a general form,

$$H' = \sum_{k,l,\sigma,\sigma'} h_{k\sigma l\sigma'} c_{k\sigma}^\dagger c_{l\sigma'}, \quad (5)$$

in presence of the external magnetic field the hopping parameters are modified by the Peierls phase

$$H'_B = \sum_{k,l,\sigma,\sigma'} h_{k\sigma l\sigma'} \exp \left[\frac{2\pi i}{\Phi_0} \int_{\mathbf{r}_i}^{\mathbf{r}_j} \mathbf{A} \cdot d\mathbf{l} \right] c_{k\sigma}^\dagger c_{l\sigma'} \quad (6)$$

where \mathbf{A} is the vector potential, $\Phi_0 = h/e$ is the magnetic flux quantum and \mathbf{r}_i is the position of i -th ion.

The spin-effects of the magnetic field are introduced by the Zeeman interaction

$$H'_{B,Z} = H'_B + \frac{1}{2} g \mu_B B \sum_{k,\sigma} (\hat{\mathbf{s}}_z)_{\sigma\sigma} c_{k\sigma}^\dagger c_{l\sigma}, \quad (7)$$

with μ_B the Bohr magneton and $g = 2$.

B. Quantum rings: induced at the n-p junction and side-attached

In order to form an n-p junction within the ribbon we introduce an external potential of e.g. a charged tip

of an atomic force microscope [44, 45, 59] – see Fig. 2. The original tip potential is of the Coulomb form which is screened by deformation of the electron gas within the conducting plane. The Schrödinger-Poisson equations for the tip screened by the two-dimensional electron gas produce an effective tip potential [59] which is close to the Lorentz form

$$W(x, y) = \frac{V_t}{1 + [(x - x_t)^2 + (y - y_t)^2]/d^2}, \quad (8)$$

where x_t, y_t is the tip position over the plane, and d is the effective width of the tip potential that is of the order of the tip-electron gas distance [59]), and V_t depends on the charge accumulated by the tip. We adopt $V_t = 400$ meV and $d = 4.92$ nm as in the previous paper [44]. In Hamiltonian H_0 given by Eq. (1), $W_i = W(x_i, y_i)$. For the workpoint we set $E_F = 60$ meV with the fluorine concentration $\eta = 0.5\%$ unless stated otherwise.

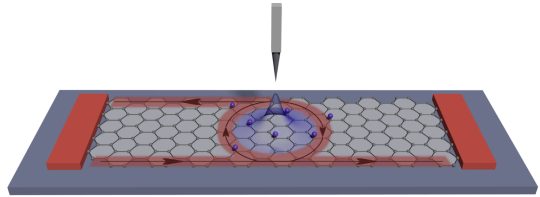


FIG. 2. The nanoribbon with F adatoms, and the n-p junction introduced by a tip of an atomic force microscope. The p region is induced below the tip. The arrows show the orientation of the edge and junction currents for the magnetic field oriented from above to the graphene plane.

In presence of the Zeeman effect large spin-flips can be obtained when the electron path remains the same for both spin orientations. We arrange for these conditions with a quantum ring side attached to the ribbon – see Fig. 3. The ribbon that is 293 atoms wide is considered for this purpose. The external and internal radii of the ring are 27 nm and 63 nm, respectively, and the arm of the ring contains about 293 atoms along its radius. The fluorine is adsorbed only within the ring.

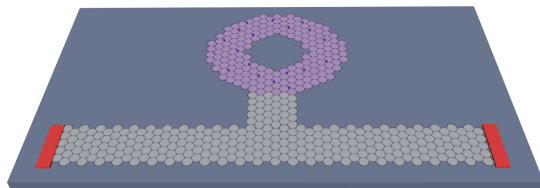


FIG. 3. Schematics of a fluorinated quantum ring side-attached to the graphene ribbon.

C. Solution of the scattering problem

1. Implementation of the Landauer approach

Outside the scattering region the nanoribbon does not contain adatoms, so that the input and the output leads, i.e., the left and right ends of the ribbon, respectively, are free of the spin-orbit interaction. The eigenstates of the leads are spin-independent and are determined in the Bloch form

$$\psi_{u,v,\sigma}^{k_m} = \chi_{v,\sigma}^{k_m} e^{ik_m u \Delta x}, \quad (9)$$

where k_m is the wave vector for m -th subband, u numbers the elementary cells of the ribbons, and v numbers the atoms inside the elementary cell. The wave function in the input lead is a superposition of the incident electron states with wave vectors k^+ and backscattered states with wave vectors k^- ,

$$\Psi_{u,v,\sigma}^{in} = \sum_l \left(c_{in}^l \chi_{v,\sigma}^{k_l^+} e^{ik_l^+ u \Delta x} + d_{in}^l \chi_{v,\sigma}^{k_l^-} e^{ik_l^- u \Delta x} \right), \quad (10)$$

where the summation over l runs over the subbands appearing at the Fermi level. At the output channel we have only the transferred, right-going waves

$$\Psi_{u,v,\sigma}^{out} = \sum_l c_{out}^l \chi_{v,\sigma}^{k_l^+} e^{ik_l^+ u \Delta x}. \quad (11)$$

We solve for the scattering wave function Ψ that is an eigenstate of the Hamiltonian for an assumed Fermi energy that is glued to the boundary conditions given by Eqs. (10) and (11) for each incoming subband separately setting $c_{in}^l = \delta_{lm}$, for the electron incident from the subband m . We use the wave function matching method [60], which produces the scattering amplitudes for the reflected (d_{in}) and transferred (c_{out}) waves.

For the Hamiltonian in form (6) the current flowing along the π bonds between m and n ions is calculated as

$$J_{k\sigma l\sigma'} = \frac{i}{\hbar} \sum_{\sigma,\sigma'} [h_{k\sigma l\sigma'} \Psi_{k,\sigma}^* \Psi_{l,\sigma'} - h_{l\sigma' k\sigma} \Psi_{l,\sigma'}^* \Psi_{k,\sigma}], \quad (12)$$

where $\Psi_{n,\sigma}$ is the σ spin component of the wave function at the n -th ion. The formula (12) accounts for the transfer of the current from one component of the spin to the other provided that the Hamiltonian contains the spin-orbit coupling components. This is indeed the case near the adatoms. Outside the fluorinated area the spin currents are conserved and can be calculated from Eq (12) for each component of σ_z .

We calculate the current fluxes outside the fluorinated area, at the ends of the ribbon which serve as the input and output leads,

$$\phi = \sum_{\sigma m, n m} J_{m\sigma n m \sigma}, \quad (13)$$

where m are the indices of the atoms across the ribbon and n_m are their left (right) nearest neighbors in the ribbon left (right) lead where the flux is calculated. The electron transfer probability from the subband n to the subband m is calculated as

$$T_{mn} = \left| \frac{c_{out}^m}{c_{in}^n} \right|^2 \left| \frac{\phi_{k_m^+}}{\phi_{k_n^+}} \right|, \quad (14)$$

$$(15)$$

where c_{out}^m and c_{in}^n are the scattering amplitudes of the transferred wave function and incident wave functions, in the m and n modes, respectively. The overall transfer probability from the n -th subband is $T_n = \sum_m T_{mn}$, which is used in the Landauer formula for conductance

$$G = G_0 \sum_n T_n, \quad (16)$$

where $G_0 = e^2/h$ is the flux quantum. In the following we set the incident electron spins and the Bloch functions in the leads as eigenstates of the σ_z operator. We calculate the spin conserving G_{uu} , G_{dd} , and spin flipping conductance contributions G_{ud} and G_{du} by summation of T_{mn} with respect to the two spin orientations, where d and u stand for the σ_z eigenstates with eigenvalues -1 and $+1$, respectively.

2. Boundary conditions

Boundary conditions for left (input) and right (output) lead was calculated using Wave Function Matching (WFM) method [60]. The Hamiltonian matrix for infinite ribbon that serves as the input or output lead to the scattering region can be put in form

$$\mathcal{H} = \begin{pmatrix} \ddots & \dots & 0 & 0 & \\ \vdots & \mathbf{H}_{u-1} & \mathbf{B}_{u-1}^\dagger & 0 & 0 \\ 0 & \mathbf{B}_{u-1} & \mathbf{H}_u & \mathbf{B}_u^\dagger & 0 \\ 0 & 0 & \mathbf{B}_u & \mathbf{H}_{u+1} & \vdots \\ & 0 & 0 & \dots & \ddots \end{pmatrix}, \quad (17)$$

where matrix \mathbf{H}_u is the Hamiltonian of single elementary cell u , matrix \mathbf{B}_u describes connections between cells u and $u+1$. Matrices \mathbf{H}_u and \mathbf{B}_u are the size of $2n \times 2n$ where n is the orbital number for the atom inside elementary cell (factor 2 arise from spinor splitting). For an ideal periodic infinite ribbon matrices \mathbf{H}_u and \mathbf{B}_u are identical, therefore the u symbol will be omitted from this point. The eigenfunction of the Hamiltonian \mathcal{H} can

be divided on eigenfunctions for each elementary cell

$$\boldsymbol{\psi} = \begin{pmatrix} \vdots \\ \psi_{u-1} \\ \psi_u \\ \psi_{u+1} \\ \vdots \end{pmatrix} \quad (18)$$

where ψ_u is the vector of size $2n$ (n orbitals for each spinor). The wave function satisfies the equation

$$-\mathbf{B}\psi_{u-1} + (\mathbf{E}\mathbf{I} - \mathbf{H})\psi_u - \mathbf{B}^\dagger\psi_{u+1} = 0. \quad (19)$$

Using Bloch form of the wave function (9) in substitution

$$\psi_{u-1} = \chi, \quad \psi_u = \lambda\chi, \quad \psi_{u+1} = \lambda^2\chi,$$

where $\lambda = \exp(ik\Delta x)$, we get

$$-\mathbf{B}\chi + \lambda(\mathbf{E}\mathbf{I} - \mathbf{H})\chi - \lambda^2\mathbf{B}^\dagger\chi = 0, \quad (20)$$

For $\eta = \lambda\chi$ equation (20) above can be written as

$$\left[\begin{pmatrix} 0 & \mathbf{I} \\ -\mathbf{B} & \mathbf{E}\mathbf{I} - \mathbf{H} \end{pmatrix} - \lambda \begin{pmatrix} \mathbf{I} & 0 \\ 0 & \mathbf{B}^\dagger \end{pmatrix} \right] \begin{bmatrix} \chi \\ \eta \end{bmatrix} = 0. \quad (21)$$

Described eigenproblem has $4n$ solutions: $2n$ left-going and $2n$ right-going modes - decaying or propagating. It is straightforward to identify right and left going evanescent modes. The eigenvalue satisfies $|\lambda_{n,\sigma}| < 1$ for right-going evanescent modes and $|\lambda_{n,\sigma}| > 1$ for left-going evanescent modes. For the propagating modes of Bloch waves the eigenvalue satisfies $\lambda_{n,\sigma} = \exp(ik\Delta x)$, with real k , hence $|\lambda_{n,\sigma}| = 1$. Then we look for values of $|\lambda| = 1$ for a given E and determine the corresponding wave vectors and periodic functions χ .

3. Calculation of the scattering amplitudes

Transmission and reflection probabilities are calculated using scattering coefficients c_{out}^l and d_{in}^l , respectively. The scattering wave function in the left output lead takes the form

$$\Psi_{0,v,\sigma}^{in} = c_{in}\chi_{v,\sigma}^{k_{in}^+} + \sum_l d_{in}^l\chi_{v,\sigma}^{k_l^-},$$

where the term with c_{in} describes the incident electron and the sum stands for the superposition of the backscattered electron waves. We calculate the derivative of the wave function

$$\begin{aligned} \frac{1}{\Delta x}(\Psi_{0,v,\sigma}^{in} - \Psi_{-1,v,\sigma}^{in}) &= \sum_l c_l\chi_{v,\sigma}^{k_l^+} \frac{1}{\Delta x}(1 - e^{-ik_l^+\Delta x}) + \\ &\sum_l d_{in}^l\chi_{v,\sigma}^{k_l^-} \frac{1}{\Delta x}(1 - e^{-ik_l^-\Delta x}), \end{aligned} \quad (22)$$

from where we get the equation for the wave function outside the computational box

$$\Psi_{-1,v,\sigma}^{in} = \Psi_{0,v,\sigma}^{in} - \sum_l c_l\chi_{v,\sigma}^{k_l^+}\Delta_{k_l^+} - \sum_l d_{in}^l\chi_{v,\sigma}^{k_l^-}\Delta_{k_l^-}. \quad (23)$$

Using scalar product for the wave function in the first cell and the function $\chi^{k_{l'}}$ we obtain

$$\langle \chi_{v,\sigma}^{k_{l'}} | \Psi_{0,v,\sigma}^{in} \rangle = \sum_l c_l \langle \chi_{v,\sigma}^{k_{l'}} | \chi_{v,\sigma}^{k_l^+} \rangle + \sum_l d_{in}^l \langle \chi_{v,\sigma}^{k_{l'}} | \chi_{v,\sigma}^{k_l^-} \rangle, \quad (24)$$

where $\langle A|B \rangle = \sum_v A_v^* B_v$ denote the inner product in discrete form. Defining matrices $\mathbf{B}_{l',l} = \langle \chi_{v,\sigma}^{k_{l'}} | \chi_{v,\sigma}^{k_l^+} \rangle$, $\mathbf{S}_{l',l} = \langle \chi_{v,\sigma}^{k_{l'}} | \chi_{v,\sigma}^{k_l^-} \rangle$ and the vector $\mathbf{A}_{l'} = \langle \chi_{v,\sigma}^{k_{l'}} | \Psi_{0,v,\sigma}^{in} \rangle$ we can rewrite Eq. (24) in a matrix form

$$\mathbf{A} = \mathbf{B}\mathbf{c}_{in} + \mathbf{S}\mathbf{d}_{in}, \quad (25)$$

which satisfies

$$d_{in}^l = \sum_{l'} (\mathbf{S}^{-1})_{l,l'} \mathbf{A}_{l'} - \sum_{l',j} (\mathbf{S}^{-1})_{l,j} \mathbf{B}_{j,l'} \mathbf{c}_{in}^{l'}. \quad (26)$$

Using Eq. (26) in Eq. (24) we obtain the left boundary condition. For the right end (N cell) the wave function

$$\Psi_{N,v,\sigma}^{out} = \sum_l c_{out}\chi_{v,\sigma}^{k_l^+} e^{-iNk_l^-\Delta x}. \quad (27)$$

Using similar approach to the right end of the computational box

$$\begin{aligned} \frac{1}{\Delta x}(\Psi_{N+1,v,\sigma}^{out} - \Psi_{N,v,\sigma}^{out}) &= \sum_l c_{out}^l\chi_{v,\sigma}^{k_l^+} \frac{1}{\Delta x} e^{iNk_l^+\Delta x} (e^{ik_l^-\Delta x} - 1) \\ &= \sum_l c_{out}^l\chi_{v,\sigma}^{k_l^+} \frac{1}{\Delta x} e^{iNk_l^+\Delta x} \Delta'_{k_l^+}, \end{aligned} \quad (28)$$

from which we get the wave function outside the right side of the computational box

$$\Psi_{N+1,v,\sigma}^{out} = \Psi_{N,v,\sigma}^{out} + \sum_l c_l\chi_{v,\sigma}^{k_l^+} e^{iNk_l^+\Delta x} \Delta'_{k_l^+}. \quad (29)$$

Using scalar product

$$\begin{aligned} \langle \chi_{v,\sigma}^{k_l^\dagger} e^{iNk_l^\dagger \Delta x} | \Psi_{N,v,\sigma}^{out} \rangle &= \sum_l c_{out}^l \langle \chi_{v,\sigma}^{k_l^\dagger} e^{iNk_l^\dagger \Delta x} | \chi_{k_l^\dagger} e^{-iNk_l^\dagger \Delta x} \rangle \text{cell.} \\ &= \sum_l \mathbf{S}'_{l',l} c_{out}^l, \end{aligned} \quad (30)$$

we get

$$c_{out}^l = (\mathbf{S}'_{l',l})^{-1} \langle \chi_{v,\sigma}^{k_l^\dagger} e^{iNk_l^\dagger \Delta x} | \Psi_{N,v,\sigma}^{out} \rangle. \quad (31)$$

III. RESULTS AND DISCUSSION

A. Accumulation of the spin precession events ($B = 0$)

As a proof of principle for accumulation of the local spin precession events we consider a narrow ribbon depicted in Fig. 4.

The ribbon is a sequence of hexagons with the fluorine atoms placed near the junctions of one hexagon to the other [Fig. 4]. No external magnetic field is applied and the electron is injected to the system with spin-down orientation from the left-hand side. The positions of the F atoms are repeated periodically within the ribbon, so the G dependence on E_F forms a series of resonances as for a superlattice band filter [61]. We set the value of the Fermi energy $E_F = 4.620512$ eV marked by the dot in Fig. 5 for which the system is transparent for electrons and look at the average spin z and x components calculated for subsequent hexagonal elementary cells of the ribbon in Fig. 6. For the resonant energy electron on its way across the system comes to fluorinated carbon atom with the same momentum and no backscattering is present. In total there are 400 F atoms along the ribbon with the concentration $\eta \approx 6.7\%$. The overall conductance G and the spin-flip contribution are depicted in Fig. 5.

Although an effect of a single fluorine atom to the orientation of the electron spin is very small we can see that upon transition below 400 fluorine atoms within the system which is nearly enough to rotate the electron spin from the $-z$ the $+z$ orientation. The source of the spin-flip transfer in the considered system is the Rashba component of the Hamiltonian that is due to the local electric field introduced by adatoms.

The Rashba spin-orbit interaction due to the adatom introduces an effective magnetic field [64] $\mathbf{B}_{SO} = C(\mathbf{p} \times \mathbf{E})$ [64], where C is a constant, \mathbf{p} the electron momentum and \mathbf{E} the electric field vector. For the planar motion $p_z = 0$ and the vertical electric field $E_z \neq 0$ induced by the adatom, the \mathbf{B}_{SO} is oriented along the y direction, i.e. in-plane and perpendicular to the momentum orientation. The spin of the electron moving within the graphene layer precesses around \mathbf{B}_{SO} [2, 26, 65] – in the case considered in Fig. 6 from the orientation to

below the ribbon ($-z$) through the orientation along the ribbon (x) for about 480th hexagonal cell of the ribbon to the orientation above the ribbon ($+z$) for the 960th

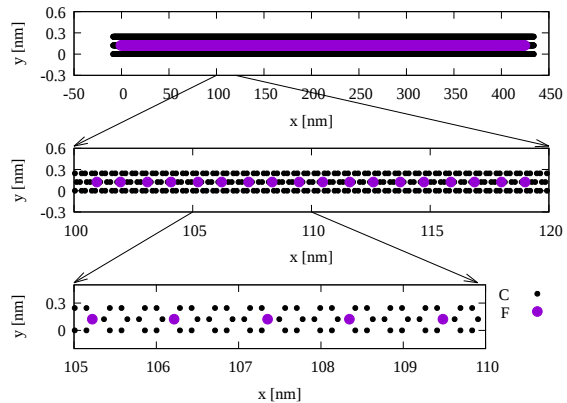


FIG. 4. A narrow ribbon that is considered in subsection III.A with the fluorine concentration $\eta \approx 6.7\%$. The position of the C and F ions are marked with black and purple dots, respectively.

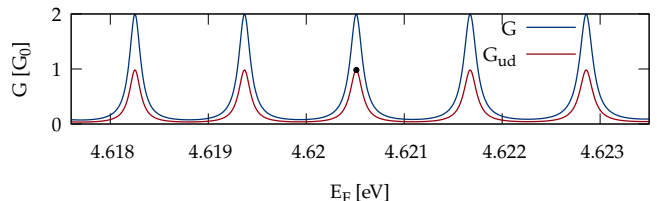


FIG. 5. The conductance G and its spin-flip contributions for the system given in Fig. 4. The narrow range of E_F was chosen to distinguish resonances.

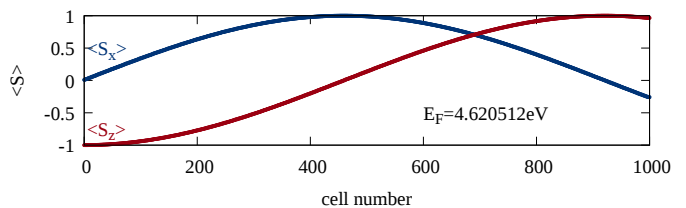


FIG. 6. The average x and z components of the spin calculated for subsequent elementary cells for $E_F = 4.620512$ eV (see the dot in Fig. 5) for which the system is transparent for the Fermi electron. The electron is incident from the left with $\mathbf{s}_z = -1$ orientation. The average y component (not shown) is nearly 0 all along the ribbon.

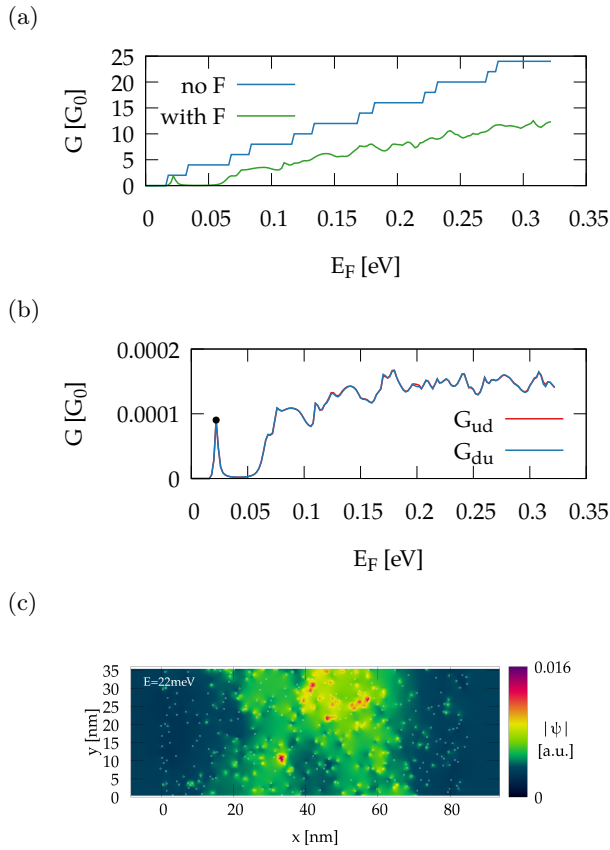


FIG. 7. (a) Conductance for a pristine semiconducting armchair nanoribbon (blue line) and the one with 400 fluorine adatoms (green line) as functions of the Fermi energy at $B = 0$. (b) The spin-flipping contribution to conductance: the probability of the spin inversion from one σ_z eigenstates to the other upon transition across the fluorinated segment. (c) The amplitude of the scattering wave function for the peak at $E = 0.022$ eV marked by the black dot in (b).

B. Transport across a fluorinated layer at $B = 0$

The results of the preceding subsection demonstrate that the spin flip is possible upon electron transition under many F adatoms. Nevertheless, an experimental fabrication of the extremely narrow ribbon with ordered F positions is rather unlikely. Let us then consider the ribbon which is 292 atoms wide with random locations of the F atoms [see Fig. 1(a)].

The calculated electron transfer probability as a function of the Fermi energy is given in Fig. 7(a). The blue line indicates the ribbon conductance in the absence of the fluorine atoms, which in G_0 units is equal to the number of subbands that carry the flux to the right. The adatoms perturb the system and induce strong backscattering, which induces the drop of conductance in Fig. 7(a) with introduction of the adatoms. In the scattering region only 0.5% of the carbon atoms are fluorinated, but the perturbation of the potential by adatoms is strong

and their random locations rule out the transparency of the system at resonances as in the ordered system of Fig. 5.

Only a very low spin-flip probability is observed [Fig. 7(b)]. A local maximum of the spin-flip probability near 0.022 eV [Fig. 7(b)] is associated with a quasi-bound resonance [Fig. 7(a)] that is supported by a group of adatoms [see the amplitude of the scattering wave function at Fig. 7(c)].

The electron backscattering by adatoms inverts the direction of the electron motion, and on the electron way back the spin precession [65] due to the local Rashba interaction is reversed [see $\Delta\varphi$ for the incident and $-\Delta\varphi$ for the backscattered motion in Fig. 8(a)], hence the near cancellation of the overall spin precession events that results in the low spin-flipping conductance contribution in Fig. 7(b).

Figure 7(b) shows that the spin-flipping effects of the electron passage across the fluorinated layer are very weak. Formation of a resonance supported by adatoms [Fig. 7(c)] with the Fermi electron experiencing a multiple scattering increases the electron dwelling time in the area where the spin-orbit coupling is present and enhances the spin-flip probability [see Fig. 7(b) near $E_F = 0.022$ eV], which however remains very low.

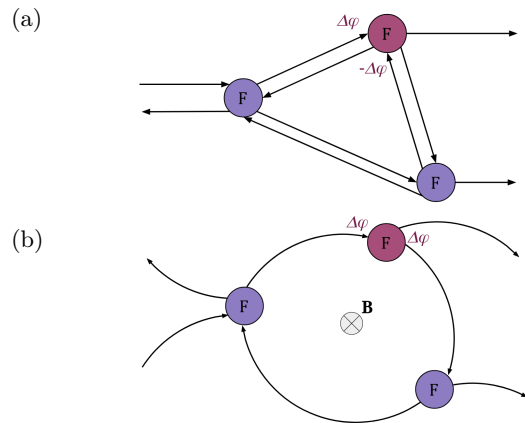


FIG. 8. Classical electron paths scattered by the fluorine adatoms (F). Electron is incident from the left. In the absence of the magnetic field (a) the electron gets backscattered and the spin precession angle $\Delta\varphi$ due to the Rashba interaction induced by a single F adatom marked by red is reversed by the backscattering $-\Delta\varphi$. In the quantum Hall conditions (b) backscattering along the same path is absent due to the magnetic deflection of the trajectories. For closed paths the precession angle accumulates at each electron transition near an adatom.

C. Recycling the electron passages: circulation around n-p junction (Zeeman interaction neglected)

In order to accumulate the effects of the spin precession we introduced a n-p junction to the system defined

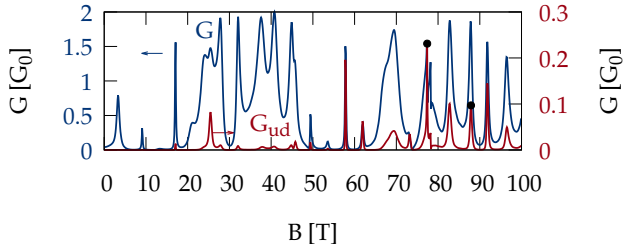


FIG. 9. The overall (left axis, blue line) conductance and its spin flipping contribution (right axis, red line) for the fluorinated n-p junction. Black dots represent peaks for which scattering densities are presented below.

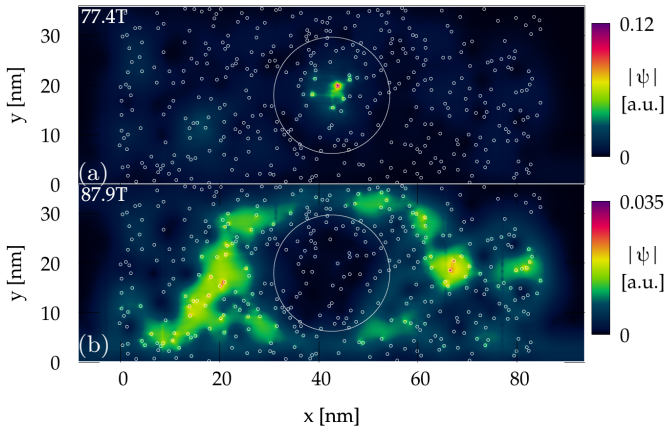


FIG. 10. The amplitude of the scattering wave function for two peaks of conductance of Fig. 9 (black dots) at 77.4 T (a) and 87.9 T (b). The circle indicates the position of the n-p junction defined by $E_F = V(x, y)$. The fluorine adatoms are marked with tiny white circles.

by a gate potential – a tip of an atomic force microscope (see Fig. 2). In the perpendicular magnetic field, it is possible to induce long-living resonances localized at the n-p junction introduced by an external gate [44]. Moreover, the electron backscattering along the same path as in Fig. 8(a) is no longer present in the quantum Hall conditions. The schematics of the current circulation in the quantum Hall conditions is given in Fig. 2.

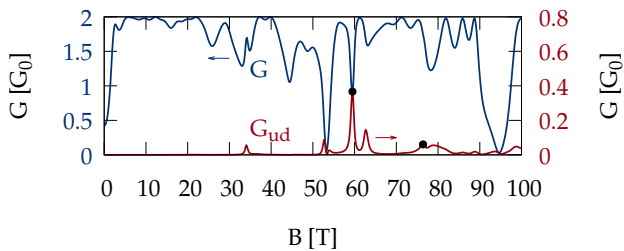


FIG. 11. Same as Fig. 9 only without the external potential defining the n-p junction.

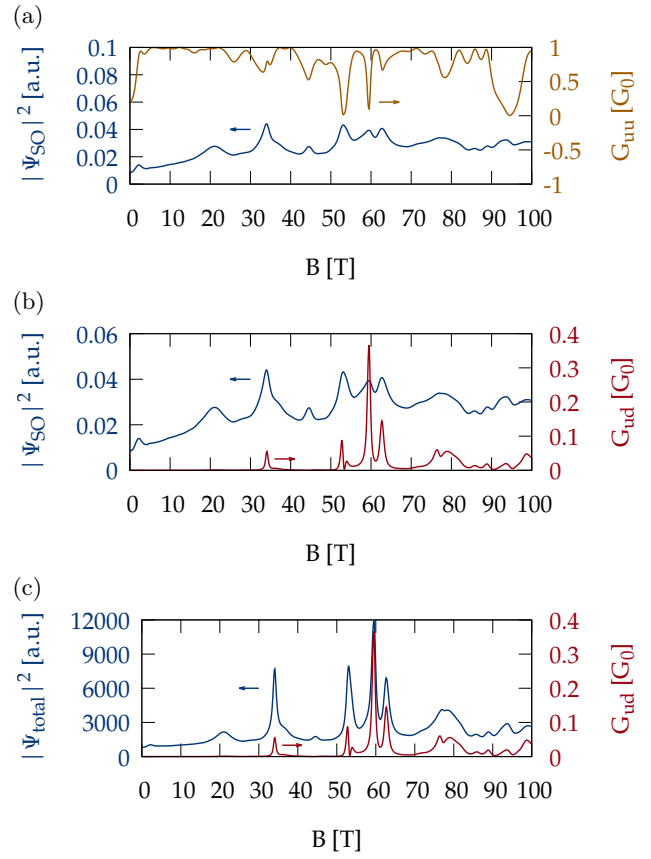


FIG. 12. (a) The spin conserving component of conductance (orange line, right axis) and the fraction of the scattering density localized in the area where the spin-orbit coupling interaction is present (blue line, left axis). (b) same as (a), only the red line indicates the spin-flipping contribution to conductance. (c) same as (b) only with the blue line that indicates the integral of the scattering density within the entire fluorinated ribbon segment for the normalized electron incidence amplitude.

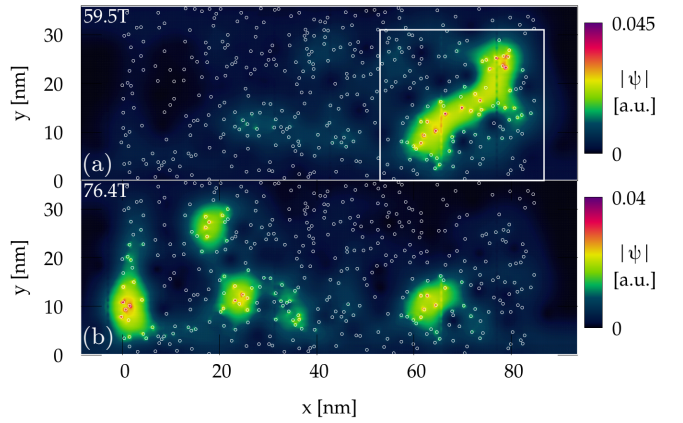


FIG. 13. The amplitude of the scattering wave function for two peaks of conductance of Fig. 11 (black dots) at 59.5 T (a) and 76.4 T (b). The fluorine adatoms are marked with tiny white circles.

For the magnetic field oriented to the graphene plane $\mathbf{B} = (0, 0, -|B|)$ the classical Lorentz force pushes the moving conduction band carriers to the right of their momentum. In consequence the incident and transferred current of conduction band electrons flows along the lower edge, while the backscattering mediated by the circular n-p junction goes through the upper edge. For the considered magnetic field orientation the current circulation around the n-p junction is clockwise (see Fig. 2), and the currents are stabilized for this single current orientation only [45]. Formation of the waveguide at the n-p junction separated from the edge of the ribbon requires formation of the quantum Hall conditions. The separation of the edge and junction current occurs when a cyclotron radius fits between the edge and the junction. For the cyclotron orbit given by the magnetic length $l_B = \sqrt{\hbar/eB} = 26[\text{nm}]/\sqrt{B[\text{T}]}$, the ribbon width w and the diameter of the junction d , the condition reads $2l_B < (w - d)/2$, which for the ribbon with 292 atoms considered here produces the condition $B > 12$ T.

In this subsection we introduce external magnetic field with Hamiltonian H'_B . The spin Zeeman effect is introduced later.

For the fluorine atoms present the conductance undergoes oscillations [Fig. 9] which are not as perfectly periodic as for the clean ribbon [44], nevertheless an approximate periodicity at higher B can be noticed. The contribution to the conductance from the spin-flip transfer is – at higher magnetic field – large, reaching $0.2G_0$. Moreover, the spin flips – at higher B – become periodic and correlated with the conductance maxima [cf. Fig. 9]. Note, that the maximal spin-flip transfer probability is increased by as much as three orders of magnitude with respect to Fig. 7(b).

Figure 10 shows the scattering charge density at the carbon atoms for 77.4T and 87.9 T - for which the spin-flipping contribution to conductance presents local maxima [Fig. 9]. Figure 10(b) presents a typical scattering density distribution for the resonances encircling the n-p junction perturbed by the adatoms. In Fig. 10(a) a localization of the resonance at an adatom in the central – p conductivity – region can be seen. The resonances localized inside potential barrier were discussed in Ref. 44. Their long lifetime results from the direction of current circulation [44] that the Lorentz force shifts to the center of the barrier and keeps the scattering density off the n-p junction.

Note, that the peaks of the overall conductance [Fig. 9(a)] and its spin-flipping contribution [Fig. 9(b)] are correlated already for $B \geq 10$ T and the spin-flipping peaks increase in amplitude for higher B . This results from an increasing magnetic confinement of the currents near the edge and the junction which decreases the coupling between the edge currents and the circular junction currents [Fig. 2] [44, 45]. The effect results in reduction of the coupling of the n-p junction to the edge. The lifetime of the resonances is increased along with the effects of the accumulation of the spin precession phase shifts.

D. Resonances in the disordered sample (Zeeman interaction neglected)

The conductance with the external potential of the precedent section removed is plotted in Fig. 11. We observe an aperiodic dependence of conductance as a function of the external magnetic field. A conductance dip at $B = 0$ [Fig. 12(a)] is characteristic to the weak localization as for a disordered conductor. In graphene the weak localization dip is observed when the intervalley scattering is strong [46]. In the present paper the role of the atomic scale defects that induce the intervalley scattering is played by the adatoms themselves. The intervalley scattering length can be estimated by the average distance between the F atoms which is $\simeq 1.5$ nm for the dilute 0.5% F concentration. In the present paper we consider ideal edges of the ribbons. The defects of the edge introduce additional intervalley scattering in addition to the adatoms. When the edge is defected the peaks of conductance for nonzero B change in position and the weak-localization dip varies in depth but the $G(B)$ dependence is not qualitatively changed.

In perpendicular external magnetic field the resonances supported by the adatoms are also associated with current circulation from one scattering event to the other, and the backscattering along the same path which limits the spin precession effects does not occur [Fig. 8(b)] due to the Lorentz forces. This opens a chance for accumulation of the spin precession effects as for circular n-p junction. High peaks of the spin-flipping contribution to conductance are found [Fig. 12(b)] with irregular positions at the B scale. The peaks of spin flipping conductance are now correlated with the dips of the spin-conserving conductance in contrast to the results obtained for the circular n-p junction discussed above. The scattering density in the absence of the n-p junction exhibits localization of the quasi-bound states [Fig. 13] varying between one resonance and the other.

We searched for the relation between the form of the scattering density, the conductance and its spin-resolved contributions. In Fig. 12(a,b) the blue line shows the relative contribution of the scattering density at the fluorinated carbon atom and its neighbors to the overall scattering density inside the computational box. In Fig. 12(a) we can see that the transfer probability is minimal when the density localization around the fluorinated carbon atoms is large. On the other hand, the spin-flip transfer probability [Fig. 12(b)] is maximal when the scattering density near the fluorinated atoms is large [Fig. 12(b)]. The results are due to the fact that the fluorine atoms are both sources of backscattering and the spin flips. We found [Fig. 12(c)] a much closer correlation of the spin-flip transfer probability with the ratio of the scattering density localized within the entire fluorinated region. In the present approach the incident electron density is normalized and kept constant for any B . The system of the adatoms for some values of the magnetic field supports a long living resonance at the Fermi energy. In these condi-

tions the scattering density within the fluorinated region acquires large values. The integral of the scattering density [Fig. 12(c)] over the fluorinated region reproduces very closely the shape the spin-flip transfer probability as a function of the magnetic field.

E. Wide ribbons and the Zeeman interaction

Formation of the current confinement at the n-p junction or resonances supported by adatoms presented above were due to the orbital effects of the external magnetic field that for the thin ribbon 292 atoms wide appeared only for the fields of the order of 50 T. In order to shift the magnetic field scale to lower values the wider ribbon is needed. The conductance for the fluorinated ribbon of width 125 nm is plotted in Fig. 14(a), still without the Zeeman interaction. The spin-flips occur already for B of the order of 10 T and are correlated with formation of localized resonances within the fluorinated ribbon segment (Fig. 14(b)).

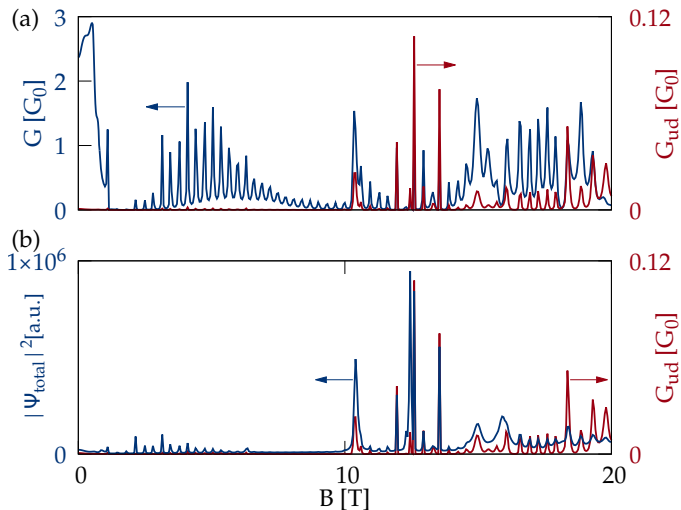


FIG. 14. (a) Conductance (G) and its spin-flipping contribution G_{ud} for a wide nanoribbon with 1017 atoms across and width 125 nm for $E_F = 30$ meV (b) G_{ud} versus the integral of the wave function within the fluorinated area. Zeeman interaction is neglected.

All the results presented above were obtained without the spin Zeeman effect. Figure 15 shows the conductance as a function of the external magnetic field with the Zeeman interaction. The peaks of G_{ud} appear but reduced by a factor of $\simeq 10$. Similarly, for the n-p junctions induced by external potential the spin-flipping contribution to conductance is drastically reduced by the spin Zeeman interaction. In presence of the spin Zeeman interaction for the perpendicular magnetic field the electron spin on its motion from one adatom to the other precesses with respect to the z axis. This precession does not change the average $\langle S_z \rangle$ value, only the perpendicular components $\langle S_x \rangle$ and $\langle S_y \rangle$ are affected. The spin precession length at

10 T is 1.785 μm , i.e. by orders of magnitude larger than the average distance between the F-F adatoms ($\simeq 1.5$ nm). The effect behind the reduction of the spin flipping conductance with the Zeeman interaction is the spin dependent Fermi wave vector. In the disordered sample the scattering wave function is very sensitive to the value of the Fermi wave vector and the accumulation of the spin precession events requires that the electron stays on its path while its spin is rotated. This is no longer the case when the spin Zeeman effect is present. The solution to this problem is given in the next subsection.

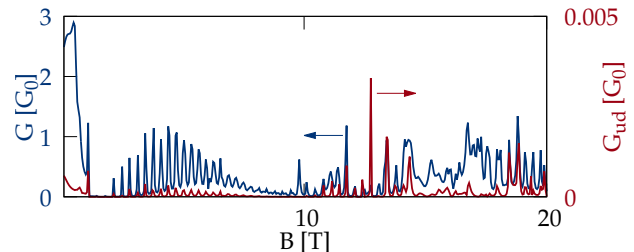


FIG. 15. Same as (a) in presence of the Zeeman interaction.

F. Side-attached quantum rings

A way to keep the electron on its path while the spin is rotated is the application of a lateral confinement of e.g. quantum ring as in Fig. 3. The quantum ring [45] supports localized resonances with the current circulation of a fixed orientation. The results for the ring attached to the thin ribbon with the Zeeman interaction is given in Fig. 16. The spin-flipping contributions to conductance acquire values in spite of the presence of the spin Zeeman interaction.

The overall conductance is a symmetric function of the external magnetic field $G(B) = G(-B)$ in consistency with the Onsager relation for a two-terminal device. Nevertheless, the spin-flipping contribution to conductance depends on the orientation of the magnetic field. The spin flips occur only for $B < 0$, i.e. for the magnetic field oriented in the $+z$ direction which injects [45, 51] the incident electron wave function from the ribbon to the quantum ring. The injection occurs only provided that a localized resonance is supported by the ring for the applied value of the magnetic field [45]. For strong magnetic field oriented in the $-z$ direction, the electron wave function is kept to the lower edge of the ribbon and does not notice the presence of the ring. This fact – with the Onsager relation – leads to $G(\pm B) = 2G_0$ limit for high magnetic fields inducing the quantum Hall conditions (see Fig. 16(a)).

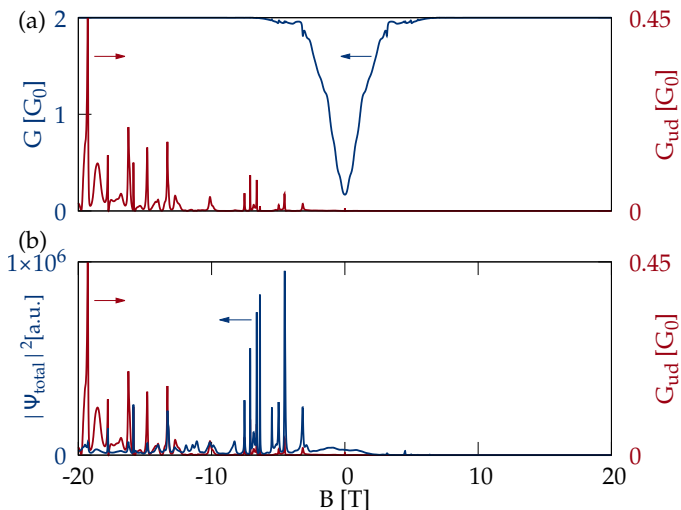


FIG. 16. (a) The conductance G and its spin-flipping contribution G_{ud} for the fluorinated quantum ring of Fig. 3 side attached to the thin channel with 293 atoms across. (b) G_{ud} versus the integral of the scattering wave function within the quantum ring. The spin Zeeman interaction is present. The calculation is for $E_F = 15$ meV and $\eta = 1\%$ concentration of the fluorine atoms with tight binding parameters taken from [22] for 7×7 supercell.

IV. SUMMARY AND CONCLUSIONS

We studied charge and spin transport across a graphene nanoribbon with dilute fluorine adatoms using

the wave function matching technique within the tight-binding approach. The electron passage below a single F adatom induces a small rotation of the electron spin due to the spin precession by a local Rashba interaction. In order to produce a spin-flip many the micro precession events at separate adatoms need to accumulate. We demonstrated that the necessary accumulation occurs when the electron circulates around a closed path in the external magnetic field in localized resonant states supported by an induced n-p junction or by the adatoms themselves. The spin-flipping effect is deteriorated by the spin Zeeman interaction which introduces the spin dependence to the electron trajectory. The dependence is of a secondary importance for a quantum ring side-attached to the nanoribbon which supports the localized resonances with a fixed electron circulation around the ring and allows for large spin-flipping contribution to conductance for the magnetic field orientation which injects the incident electron to the ring.

ACKNOWLEDGMENTS

This work was supported by the National Science Centre (NCN) according to decision DEC-2015/17/B/ST3/01161. The calculations were performed on PL-Grid Infrastructure

-
- [1] I. Zutic, J. Fabian, and S. Das Sarma, Rev. Mod. Phys. **76**, 323 (2004).
- [2] S. Datta and B. Das, Appl. Phys. Lett. **56**, 665 (1990).
- [3] A. H. Castro Neto, F. Guinea, N. M. R. Peres, K. S. Novoselov, and A. K. Geim, Rev. Mod. Phys. **81**, 109 (2009).
- [4] W. Han and R. K. Kawakami, Phys. Rev. Lett. **107**, 047207 (2011).
- [5] T. Maassen, J.J. van den Berg, N. Ijbema, F. Fromm, T. Seyller, R. Yakimova, and B.J. van Wees, Nano Lett., **12**, 1498 (2012).
- [6] A. Manchon, H.C. Koo, J. Nitta, S.M. Frolov, R.A. Duine, Nature Materials **14**, 871. (2015)
- [7] E.A. Laird, F. Kuemmeth, G. Steele, K. Grove-Rasmussen, J. Nygård, K. Flensberg, L.P. Kouwenhoven, Rev. Mod. Phys. **87**, 703 (2015).
- [8] A. Avsar, J. Y. Tan, T. Taychatanapat, J. Balakrishnan, G.K.W. Koon, Y. Yeo, J. Lahiri, A. Carvalho, A. S. Rodin, E.C.T. O'Farrell, G. Eda, A. H. Castro Neto and B. Özyilmaz, Nature Comm. **5**, 4875 (2014).
- [9] M. Gmitra, D. Kochan, P. Högl, and J. Fabian, Phys. Rev. B **93**, 155104 (2016).
- [10] V. N. Kotov, B. Uchoa, V. M. Pereira, F. Guinea, and A. H. Castro-Neto, Rev. Mod. Phys. **84**, 1067 (2012).
- [11] O. Leenaerts, B. Partoens, and F.M. Peeters, Phys. Rev. B **80**, 24522 (2009).
- [12] J. J. Palacios, J. Fernández-Rossier, L. Brey. Phys. Rev. B **77**, 195428, (2008).
- [13] P. Haase, S. Fuchs, T. Pruschke, H. Ochoa, and F. Guinea. Phys. Rev. B. **83**, 241408 (2011).
- [14] N. A. Pike, D. Stroud. Phys. Rev. B **89**, 115428 (2014).
- [15] F. Gargiulo, G. Autès, N. Virk, S. Barthel, M. Rosner, L.R.M. Toller, T.O. Wehling, and O. Yazyev. Phys. Rev. Lett. **113**, 2476601 (2014).
- [16] J. Zhou, Q. Wang, Q. Sun, X.S. Chen, Y. Kawazoe and P. Jena. Nano Lett. **9**, 3867, (2009).
- [17] M. Sepioni, R.R. Nair, S. Rablen, J. Narayanan, F. Tuna, R. Winpenny, A.K. Geim, and I. R. Grigorieva. Phys. Rev. Lett. **105**, 207205 (2010).
- [18] X. Hong, S.-H. Cheng, C. Herding, and J. Zhu, Phys. Rev. B **83**, 085410 (2011).
- [19] R. R. Nair, M. Sepioni, I.-L. Tsai, O. Lehtinen, J. Keinonen, A. V. Krasheninnikov, T. Thomson, A. K. Geim, and I. V. Grigorieva, Nat. Phys. **8**, 199 (2012).
- [20] X. Hong, K. Zou, B. Wang, S.-H. Cheng, and J. Zhu, Phys. Rev. Lett. **108**, 226602 (2012).
- [21] H. Santos and L. Henrard, J. Phys. Chem. C **118**, 27074 (2014).

- [22] S. Irmer, T. Frank, S. Putz, M. Gmitra, D. Kochan, and J. Fabian, *Phys. Rev. B* **91**, 115141 (2015).
- [23] R. R. Nair, M. Sepioni, I.-L. Tsai, O. Lehtinen, J. Adam A. Stabile, Aires Ferreira, Jing Li, N. M. R. Peres, and J. Zhu, *Phys. Rev. B* **92**, 121411(R) (2015).
- [24] A. Sadeghi, M. Neek-Amal, G. R. Berdiyrov, and F. M. Peeters, *Phys. Rev. B* **91**, 014304 (2015).
- [25] K. Wakabayashi, Y. Takane, M. Yamamoto, and M. Sigrist, *Carbon* **47**, 124 (2009).
- [26] P. Chuang, S.-C. Ho, L. W. Smith, F. Sfigakis, M. Pepper, C.-H. Chen, J.-C. Fan, J. P. Griffiths, I. Farrer, H. E. Beere, G. A. C. Jones, D. A. Ritchie, and T.-M. Chen, *Nature Nano.* **10**, 35 (2015).
- [27] D. A. Abanin and L. S. Levitov, *Science* **317**, 641 (2007).
- [28] J. R. Williams, L. DiCarlo, and C. M. Marcus, *Science* **317**, 638 (2007).
- [29] J. Tworzydło, I. Snyman, A. R. Akhmerov, and C. W. J. Beenakker, *Phys. Rev. B* **76**, 035411 (2007).
- [30] J. R. Williams, T. Low, M. S. Lundstrom, and C. M. Marcus, *Nat. Nanotechnol.* **6**, 222 (2011).
- [31] A. Cresti, G. Grosso, and G. P. Parravicini, *Phys. Rev. B* **77**, 233402 (2008).
- [32] T. Taychatanapat, J. Y. Tan, Y. Yeo, K. Watanabe, T. Taniguchi, and B. Özyilmaz, *Nat. Commun.* **6**, 6093 (2015).
- [33] P. Rickhaus, P. Makk, M.-H. Liu, E. Tóvári, M. Weiss, R. Maurand, K. Richter, and C. Schönenberger, *Nat. Commun.* **6**, 6470 (2015).
- [34] K. Kolasiński, A. Mreńca-Kolasińska, and B. Szafran, *Phys. Rev. B* **95**, 045304 (2017).
- [35] J. R. Williams and C. M. Marcus *Phys. Rev. Lett.* **107**, 046602 (2011).
- [36] P. Carmier, C. Lewenkopf, and D. Ullmo, *Phys. Rev. B* **84**, 195428 (2011).
- [37] M. Barbier, G. Papp, and F. M. Peeters, *Appl. Phys. Lett.* **100**, 163121 (2012); S. P. Milovanović, M. Ramezani Masir, and F. M. Peeters, *Appl. Phys. Lett.* **105**, 123507 (2014).
- [38] N. Davies, A. A. Patel, A. Cortijo, V. Cheianov, F. Guinea, and V. I. Fal'ko, *Phys. Rev. B* **85**, 155433 (2012).
- [39] J.-C. Chen, X. C. Xie, and Q.-F. Sun, *Phys. Rev. B* **86**, 035429 (2012).
- [40] Y. Liu, R. P. Tiwari, M. Brada, C. Bruder, F. V. Kusmartsev, and E. J. Mele, *Phys. Rev. B* **92**, 235438 (2015).
- [41] T. Taychatanapat, K. Watanabe, T. Taniguchi, and P. Jarillo-Herrero, *Nat. Phys.* **9**, 225 (2013).
- [42] S. Bhandari, G.-H. Lee, A. Kales, K. Watanabe, T. Taniguchi, E. Heller, P. Kim, and R. M. Westervelt, *Nano Lett.* **16**, 1690 (2016).
- [43] M.-H. Liu, C. Gorini, and Klaus Richter, *Phys. Rev. Lett.* **118**, 066801 (2017).
- [44] A. Mreńca-Kolasińska, S. Heun, and B. Szafran *Phys. Rev. B* **93**, 125411 (2016).
- [45] A. Mreńca-Kolasińska and B. Szafran, *Phys. Rev. B* **94**, 195315 (2016).
- [46] F. V. Tikhonenko, D. W. Horsell, R. V. Gorbachev, and A. K. Savchenko *Phys. Rev. Lett.* **100**, 056802 (2008).
- [47] D. Cabosart, S. Faniel, F. Martins, B. Brun, A. Felten, V. Bayot, and B. Hackens, *Phys. Rev. B* **90**, 205433 (2014).
- [48] S. Russo, J. B. Oostinga, D. Wehenkel, H. B. Heersche, S. S. Sobhani, L. M. K. Vandersypen, and A. F. Morpurgo, *Phys. Rev. B* **77**, 085413 (2008).
- [49] D. Smirnov, J. C. Rode, and R. J. Haug, *Appl. Phys. Lett.* **105**, 082112 (2014).
- [50] M. Huefner, F. Molitor, A. Jacobsen, A. Pioda, C. Stampfer, K. Ensslin, and T. Ihn, *New J. Phys.* **12**, 043054 (2010).
- [51] J. Dauber, M. Oellers, F. Venn, A. Epping, K. Watanabe, T. Taniguchi, F. Hassler, and C. Stampfer, *Phys. Rev. B* **96**, 205407.
- [52] M. Y. Han, B. Özyilmaz, Y. B. Zhang, P. Kim, *Phys. Rev. Lett.* **98**, 206805 (2007).
- [53] Z. H. Chen, Y. M. Lin, M. J. Rooks, P. Avouris, *Physica E* **40**, 228 (2007).
- [54] M. Ewaldsson, I. V. Zozoulenko, H. Xu, and T. Heinzel, *Phys. Rev. B* **78**, 161407(R) (2008).
- [55] T.O. Wehling, M.I. Katsnelson, and A. I. Lichtenstein, *Phys. Rev. B* **80**, 085428 (2009).
- [56] R. M. Guzmán-Arellano, A. D. Hernández-Nieves, C. A. Balseiro, and Gonzalo Usaj, *Appl. Phys. Lett.* **105**, 121606 (2014).
- [57] C.L. Kane and E.J. Mele, *Phys. Rev. Lett.* **95**, 226801 (2005).
- [58] C.-C. Liu, Hua Jiang, and Yugui Yao, *Phys. Rev. B* **84**, 195430 (2011).
- [59] K. Kolasiński and B. Szafran *Physical Review B* **88**, 165306 (2013).
- [60] M. Zwierzycki, P. A. Khomyakov, A. A. Starikov, K. Xia, M. Talanana, P. X. Xu, V. M. Karpan, I. Marushchenko, I. Turek, G. E. W. Bauer, G. Brocks, and P. J. Kelly, *phys. stat. sol. (b)* **245**, 623 (2008).
- [61] C. Pacher, C. Rauch, G. Strasser, E. Gornik, F. Elsholz, A. Wacker, G. Kiesslich, and E. Schöll, *Appl. Phys. Lett.* **79**, 1486 (2001).
- [62] S. Ihnatsenka and G. Kirczenow *Phys. Rev. B* **85**, 121407(R) (2012).
- [63] N. Tombros, A. Veligura, J. Junesch, M.H.D. Guimaraes, I.J. Vera-Marun, H. T. Jonkman, and B. J. van Wees, *Nat. Phys.* **7**, 697 (2011).
- [64] L. Meier, G. Salis, I. Shorubalko, E. Gini, S. Schön, and Klaus Ensslin, *Nat. Phys.* **3**, 650 (2007).
- [65] S. Bednarek and B. Szafran, *Phys. Rev. Lett.* **101**, 216805 (2008).